Aerospace Science and Technology 54 (2016) 286–301

Contents lists available at ScienceDirect

Aerospace Science and Technology

www.elsevier.com/locate/aescte

Computational aerodynamic modeling for flight dynamics simulation of ram-air parachutes

Mehdi Ghoreyshi [a,*], Keith Bergeron [b], Adam Jirásek [a], Jürgen Seidel [a], Andrew J. Lofthouse [a], Russell M. Cummings [a]

[a] High Performance Computing Research Center, U.S. Air Force Academy, USAF Academy, CO 80840, United States
[b] US Army Natick Research, Development and Engineering Center, Natick, MA 01760, United States

ARTICLE INFO

Article history:
Received 22 October 2015
Received in revised form 15 April 2016
Accepted 22 April 2016
Available online 28 April 2016

Keywords:
Ram-air parachutes
Linear regression method
Dynamic derivatives

ABSTRACT

This work presents a step toward bridging the gap between flight dynamics simulation of ram-air parachutes and high-fidelity computational fluid dynamics. Today's parachute design codes mainly rely on the empirical or semi-empirical methods generated from wind tunnel experiments and drop tests. The outcome of this study will hopefully help to reduce the cost of experiments and drop testing in the design of future canopies and to better understand the aerodynamic characteristics of these geometries. In this work, the parachute geometries were modeled as rigid rectangular wings with an aspect ratio of two and zero anhedral angle. The wings have seven opening cells and the trailing edge is deflected or not deflected. To validate computational methods, the aerodynamic predictions of similar wings, but with closed and round inlets, are compared with experimental data available from the Subsonic Wind Tunnel at United States Air Force Academy. Total lift and drag force coefficients were measured at a Reynolds number of 1.4 million. The results show that computational predictions of fine (closed-inlet) grids match the experimental data very well up to the stall angle. Both experiments and simulations show that closed wings have sharp stalling characteristics. The aerodynamics of closed wings up to stall can be approximated by linear functions and their derivatives. The closed wings show a negative static stability with respect to changes in the angle of attack. The open wings, on other hand, have positive static stability in the longitudinal and lateral directions. The open wings exhibit highly nonlinear unsteady aerodynamic characteristics; they also stall earlier and have higher drag values than the closed wings. The aerodynamic derivatives of open and closed wings were estimated using a linear regression method and training data simulated in small-amplitude oscillations in pitch, yaw, and roll directions. While the open wings have large oscillations in aerodynamic coefficients over the yawing and rolling hysteresis loops, lateral aerodynamic derivatives of the open and closed wings are similar. Finally, the results show that model predictions are reasonably accurate for use in flight-dynamics simulations.

Published by Elsevier Masson SAS.

1. Introduction

Ram-air parachutes based on Domina Jalbert's kite design [1] are widely used in many military applications, especially in precision guided airdrop systems. These parachutes are typically low aspect ratio rectangular wings and consist of an upper and lower surface and a set of individual cells. The cells are inflated by the ram air entering through specially designed openings in the leading edge to form a gliding airfoil [2,3]. As a result, these parachutes are sometimes called parafoils, a term initially used by the University of Notre Dame to describe the combination of parachute and airfoil [4]. Parafoils have a large lift to drag ratio and therefore offer superior maneuverability when compared with round parachutes [5]. The precision landing capability of these parachutes depends on the control law design, aerodynamic performance, and aerodynamic data fidelity.

The aerodynamics of parachutes is very complex and should take into account the interactions between aerodynamic and structural analysis [6]. Note that the total canopy forces is the sum of aerodynamic forces and those transmitted to the canopy by the suspension lines [7]. The aerodynamic models used in the design of parafoils are typically empirical or semi-empirical methods generated from wind tunnel experiments and drop tests [8]. These experiments are relatively expensive and only available late in the design cycle. It is also difficult to obtain relevant data against

* Corresponding author.
E-mail address: mehdi.ghoreyshi@usafa.edu (M. Ghoreyshi).

http://dx.doi.org/10.1016/j.ast.2016.04.024
1270-9638/Published by Elsevier Masson SAS.

Nomenclature

a	speed of sound .... m/s
b	wing span .... m
C_D	drag coefficient, $D/q_\infty S$
C_L	lift coefficient, $L/q_\infty S$
C_{Mx}	roll moment coefficient, $M_x/q_\infty Sb$
C_{My}	pitching moment coefficient, $M_y/q_\infty Sc$
C_{Mz}	yaw moment coefficient, $M_z/q_\infty Sb$
C_p	pressure coefficient
C_Y	side-force coefficient, $Y/q_\infty S$
c	mean aerodynamic chord .... m
D	drag force .... N
f	frequency .... Hz
L	lift force .... N
M_x	roll moment .... N m
M_y	pitching moment .... N m
M_z	yaw moment .... N m
M	Mach number .... V/a
p, q, r	roll, pitch, and yaw rate .... rad/s
q_∞	dynamic pressure, $\rho V^2/2$ .... Pa
Re	Reynolds number, $\rho V c/\mu$
S	planform area .... m^2
V	freestream velocity .... m/s
x, y, z	aircraft position coordinates
Greek	
α	angle of attack .... rad or deg
$\dot{\alpha}$	time-rate of change of angle of attack .... rad/s
β	side-slip angle .... rad
$\dot{\beta}$	time-rate of change of side-slip angle .... rad/s
δ	trailing edge deflection angle .... rad
ϕ	roll (bank) angle .... rad
ρ	air density .... kg/m^3
μ	air viscosity .... kg/(m s)
ω	angular velocity .... rad/s

which drop tests or computations may be compared. Slegers and Costello [9] investigated the braking responses and control of a parafoil and payload and showed that the parafoil–payload system could roll and skid by using right and left brakes. While, limited static aerodynamic data of large-scale parafoils are available, the experimental data for dynamic stability derivatives are scarce and available late in the design cycle, especially for novel concept designs. Note that dynamic stability derivatives can have significant effects on the parafoil motion.

Parafoil aerodynamic characteristics might be estimated using the wing theory. Lingard's work [10,11], in particular, provides reasonable estimates of ram-air parachute aerodynamics including static and dynamic stability derivatives. The lift is predicted from the lifting line theory. The drag coefficient is also estimated and includes the effects of the payload, the suspension line, and the open inlet. The drag coefficient of an open inlet with the height of h was assumed to be $0.5h/c$, where c is the wing's chord length [12]. Suspension line drag takes into account the length of lines and assumed a drag coefficient of one [12]. However, these estimation methods are not accurate for unsteady flows and novel configurations such as bleed air spoilers [13–15]. These observations provide motivation to move towards Computational Fluid Dynamics (CFD) simulations because CFD modeling, in principle, can capture the flow field effects of relatively complicated geometries.

More recently, CFD has been used to simulate the flow field around ram-air parachutes [8,16,17]. These studies are mainly limited to two-dimensional airfoils or to investigate the flow-field around parachutes rather than to generate aerodynamic models for flight dynamics simulation. In addition, CFD simulations of these parachutes require special treatment. CFD solutions of parachute canopies are unsteady and nonlinear due to the cavity inside the wing [17]. Also, CFD simulations of open-inlet wings (as seen in parafoils) typically take a longer time to reach the steady-state solution than a closed wing. The solution of an open-inlet geometry has large-amplitude oscillations in lift and drag coefficients which last for a long time. Again, this physical behavior is related to the flow inside cavity. The shear layer separating the cavity and external flows induces large pressure fluctuations inside the cavity which causes large oscillations in forces-moments. As time progresses, the streamwise pressure gradients inside cavity become smaller which dampens these oscillations. As the solution reaches the steady-state conditions, the flow inside the cavity will take a uniform pressure everywhere (stagnation pressure). Finally, the CFD solutions of open airfoils are very sensitive to the quality of mesh on the external wing surfaces [18].

The objective of the present study is the generation of aerodynamic models for flight simulation of ram-air parachutes. The parachute geometries were modeled as rigid rectangular wings with an aspect ratio of two and zero anhedral angle. The anhedral angle effects on parachute aerodynamics were studied numerically and experimentally by Eslambolchi and Johari [19] and Cook et al. [20]. The experimental data showed that by adding the anhedral angle the lift produced by the wing was slightly decreased. These effects are not considered in this work.

The wings have seven open cells and the trailing edge is deflected or not deflected; deflections are asymmetric. To validate computational methods, the aerodynamic predictions of similar wings, but with closed round inlets, are compared with experimental data available from the Subsonic Wind Tunnel at United States Air Force Academy. A stability-derivative aerodynamic model was used to model wing aerodynamics; these derivatives are estimated using a linear regression method. The work is organized as follows: the first section reviews a regression method for aerodynamic modeling of open and closed wings. The CFD flow solvers are next described. Test cases, the computational grids, and experimental setup are presented next. The results are then presented and discussed, followed by concluding remarks.

2. Linear regression method

The linear regression method [21,22] is used in this work to estimate aerodynamic derivatives of ram-air parachutes. For small-amplitude motions, the aerodynamic coefficients are expressed in terms of classical stability derivatives as:

$$C_j = C_{j0} + C_{j_\alpha}\alpha + C_{j_\beta}\beta + C_{j_{\dot{\alpha}}}\frac{\dot{\alpha}c}{2V} + C_{j_{\dot{\beta}}}\frac{\dot{\beta}b}{2V} + C_{j_p}\frac{pb}{2V} + C_{j_q}\frac{qc}{2V} + C_{j_r}\frac{rb}{2V} + C_{j\delta}\delta \tag{1}$$

where $C_j = [C_L, C_D, C_Y, C_{Mx}, C_{My}, C_{Mz}]$ denote lift, drag, side force, roll, pitch, and yaw moment coefficients. These forces and moments are shown in Fig. 1. In Eq. (1), c is the aerodynamic chord; b is the wing span; V is the free-stream velocity; C_{j0} corresponds to the aerodynamic coefficient value at zero angles of attack and side slip; α, β denote angles of attack and side slip; $\dot{\alpha}$, $\dot{\beta}$ are time-rate of change of angle of attack and side slip angle;

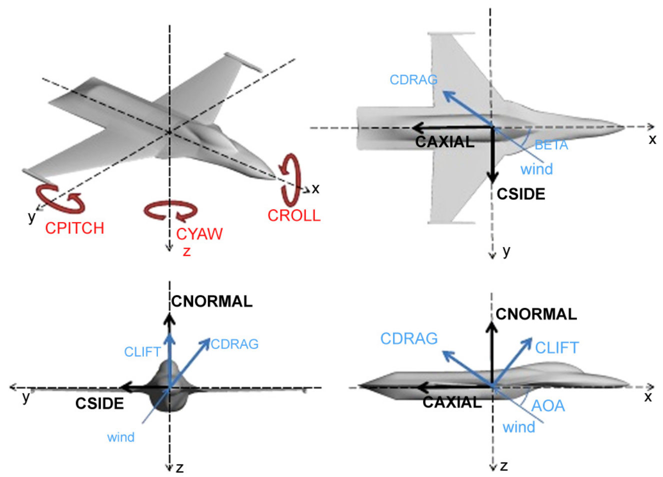

Fig. 1. Coordinate system for definition of aerodynamic forces and moments. Adapted from Ref. [38].

p, q, r are roll, pitch, and yaw rates and finally δ shows trailing-edge deflection angle. The unknown derivatives in Eq. (1) are found from CFD simulation of small-amplitude forced oscillations in the roll/pitch/yaw modes. During a forced-oscillation pitch, the lift and pitching moment can be written as:

$$C_L = C_{L0} + C_{L\alpha}\alpha + \left(C_{L\dot{\alpha}} + C_{Lq}\right)\frac{qc}{2V} \tag{2}$$

$$C_{My} = C_{My_0} + C_{My_\alpha}\alpha + \left(C_{My_{\dot{\alpha}}} + C_{My_q}\right)\frac{qc}{2V}$$

Likewise during a forced-oscillation in yaw:

$$C_Y = C_{Y0} + C_{Y\beta}\beta + \left(C_{Yr} - C_{Y\dot{\beta}}\right)\frac{rb}{2V} \tag{3}$$

$$C_{Mx} = C_{Mx0} + C_{Mx\beta}\beta + \left(C_{Mxr} - C_{Mx\dot{\beta}}\right)\frac{rb}{2V}$$

$$C_{Mz} = C_{Mz0} + C_{Mz\beta}\beta + \left(C_{Mzr} - C_{Mz\dot{\beta}}\right)\frac{rb}{2V}$$

where the minus sign in combined terms means that a positive yaw rate will decrease the wing's side-slip angle. Finally, during a forced-oscillation in roll, the aerodynamic coefficients are found as:

$$C_Y = C_{Y0} + C_{Y\beta}\beta + C_{Yp}\frac{pb}{2V} \tag{4}$$

$$C_{Mx} = C_{Mx0} + C_{Mx\beta}\beta + C_{Mxp}\frac{pb}{2V}$$

$$C_{Mz} = C_{Mz0} + C_{Mz\beta}\beta + C_{Mzp}\frac{pb}{2V}$$

where $p(t) = \dot{\phi(t)}$ and $\phi(t)$ is the roll or bank angle at each time instant. Note that the side-slip angle of $\beta(t)$ is related to the bank angle of $\phi(t)$ as:

$$\beta(t) = -\sin^{-1}(\sin\alpha \ \ \sin\phi(t)) \tag{5}$$

All above models are linear in structure; in general the function of y could be written in form of a linear mathematical model as:

$$y = \beta_0 + \beta_1 x_1 + \beta_2 x_2 + \ldots + \beta_k x_k + \epsilon \tag{6}$$

where $x_1, x_2, \ldots, x_k$ are independent inputs; $\vec{\beta} = [\beta_0, \beta_1, \ldots, \beta_k]$ is the vector of unknown coefficients and ϵ is the approximation error. Assuming there are n samples of function of y, define the vectors of $\vec{y} = [y_1, y_2, \ldots, y_n]$ and $\vec{\epsilon} = [\epsilon_1, \epsilon_2, \ldots, \epsilon_n]$. In this work $\vec{y}$ contains CFD data from forced oscillation simulations and n is the number of time steps. Independent inputs of $x_1, x_2, \ldots, x_k$ are

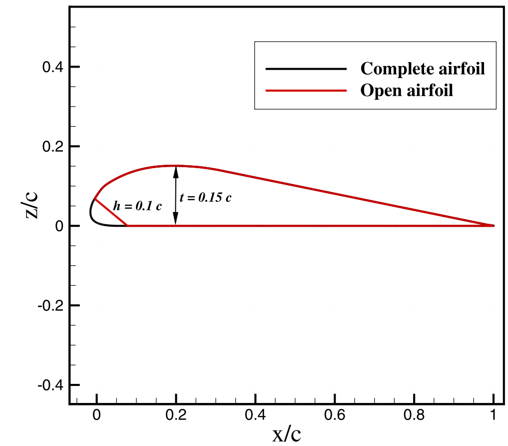

Fig. 2. The airfoil section of tested wings.

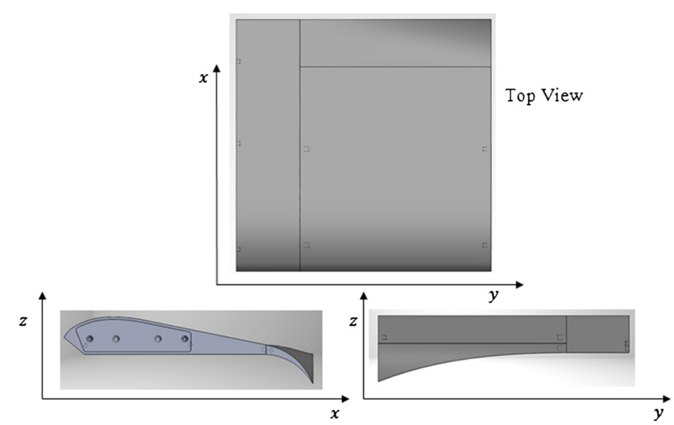

Fig. 3. CAD drawings of BF configuration.

the variables used in Eqs. (2)–(4) (e.g. α, β, ...). These variables are known at each time step of motion. The input matrix of X is then defined as:

$$\mathbf{X} = \begin{bmatrix} 1 & x_{11} & \cdots & x_{k1} \\ 1 & x_{12} & \cdots & x_{k2} \\ \vdots & \vdots & \vdots & \vdots \\ 1 & x_{1n} & \cdots & x_{kn} \end{bmatrix} \tag{7}$$

The sum of squared errors should be minimized; the squared error is:

$$S = \left(\vec{y} - X^{\mathrm{T}}\vec{\beta}\right)^{\mathrm{T}}\left(\vec{y} - X^{\mathrm{T}}\vec{\beta}\right) \tag{8}$$

The unknown parameters can then be estimated as:

$$\vec{\beta} = \left(XX^{\mathrm{T}}\right)^{-1}(X\vec{y}) \tag{9}$$

3. CFD solvers

Cobalt and CREATE$^{\mathrm{TM}}$-AV Kestrel flow solvers are used in this study. The codes are briefly described below.

3.1. Cobalt solver

The Cobalt code [23] solves the unsteady, three-dimensional and compressible Navier–Stokes equations in an inertial reference frame. The ideal gas law and Sutherland's law close the

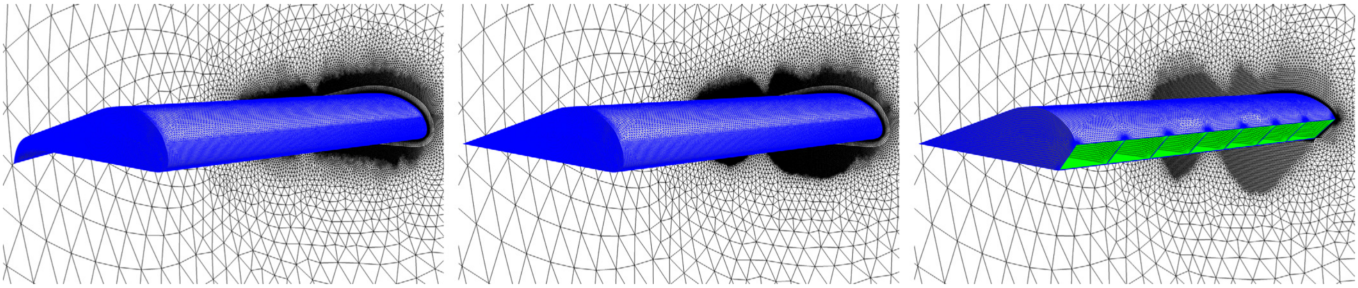

(a) Bent and Round (BR), (b) Straight and Round (SR) (c) Open and straight

Fig. 4. Computational grids. These grids are coarse using a symmetry plane and were generated by the Capstone mesh generator.

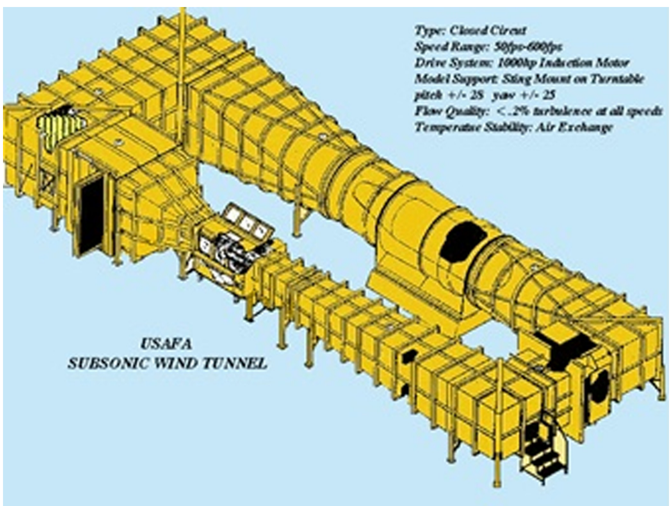

Fig. 5. The USAFA subsonic wind tunnel schematic.

system of equations and the entire equation set is nondimensionalized by free stream density and speed of sound [23]. The Navier–Stokes equations are discretized on arbitrary grid topologies using a cell-centered finite volume method. Second-order accuracy in space is achieved using the exact Riemann solver of Gottlieb and Groth [24], and least squares gradient calculations using QR factorization. To accelerate the solution of discretized system, a point-implicit method using analytic first-order inviscid and viscous Jacobians. A Newtonian sub-iteration method is used to improve time accuracy of the point-implicit method. Tomaro et al. [25] converted the code from explicit to implicit, enabling Courant–Friedrichs–Lewy numbers as high as 10^6. Some available turbulence models for Reynolds-Averaged Navier–Stokes (RANS) and delayed detached-eddy simulations (DDES) are the Spalart–Allmaras model [26], Wilcox's k–ω model [27], and Mentor's SST model [28].

3.1.1. Kestrel

Kestrel is a relatively new flow solver developed as part of the US Department of Defense Computational Research and Engineering Acquisition Tools and Environments (CREATE™), Program, which was established as a 12-year program in year 2008 and is managed by the Department of Defense (DoD) High Performance Computing Modernization Program. The goal is to enable improvements in DoD acquisition programs through the use of scalable, multidisciplinary, physics-based computational engineering software products for use on DoD high-performance computing resources [29]. CREATE consists of three computationally-based engineering tool sets for the design of air vehicles, ships and radio frequency antennae. The fixed wing analysis code, Kestrel, is part of the Air Vehicles Project (CREATE™-AV) and is a modularized, multidisciplinary, virtual aircraft simulation tool incorporating aerodynamics, structural dynamics, kinematics and kinetics [30]. The flow solver component of Kestrel (kCFD) solves the unsteady, three-dimensional, compressible Reynolds-Averaged Navier–Stokes (RANS) equations on hybrid unstructured grids [31].

In more detail, the kCFD code uses a modified Barth–Jespersen limiter [32]. The Roe's inviscid fluxes, LDD+ viscous fluxes, weighted gradients, and a vanLeer convective flux Jacobian [33] were chosen in the solver. The Gauss–Seidel scheme was then used to solve the matrix equation resulting from the implicit time integration scheme.

4. Test cases

Aerodynamic models were generated to simulate the flight dynamics of a parafoil wing with and without trailing-edge deflection. The airfoil section of the wings is shown in Fig. 2. The airfoil was provided by the Natick Soldier Research, Development, and Engineering Center (NSRDEC) and was based on a modified Clark-Y with a flat lower surface used as the cut pattern for drop tested systems [34]. The wing is characterized with an aspect ratio of two and zero anhedral angle. Several derivatives of this wing geometry were tested in the Subsonic Wind Tunnel (SWT) of United States Air Force Academy (USAFA).

These wings have either an open or closed inlet, a round or flat leading edge (for closed wings) and are with and without the trailing edge deflection. The flat leading edge wings consist of a straight line connecting the wing's lower surface to the upper surface. The TE deflection is approximately 45° as measured from the flat lower surface. For convenience, these wings were named SR, BR, SF, BF, in which S and B denote straight and bent trailing edges; R and F indicate round and flat leading edges. The CAD drawings of BF configuration are shown in Fig. 3 for more details of the bending surface.

The open wings have seven cells. All wings have the chord and wing span lengths of 300 mm and 600 mm, making the aspect ratio two. In this study, only the closed wings with a round leading-edge and the open wings are considered.

Coarse and fine RANS meshes were generated for these wings. These grids are unstructured with prismatic layers near the surfaces. Coarse grids were generated using CREATE™-MG Capstone code. The code has the capability to create and mesh geometries using the bottom-up and topdown construction methods [35]. While in the bottom-up, the construction begins with low-level entities (e.g. vertices, edges, and faces), in a top-down method, the geometry construction begins with solid regions, and performs Boolean operations such as unions and differences on the regions [35].

Capston meshes are shown in Fig. 4. These meshes are symmetric (half-span) and have around 5.7 and 10 million cells for the closed and open wings, respectively. The right trailing edge is deflected in these meshes.

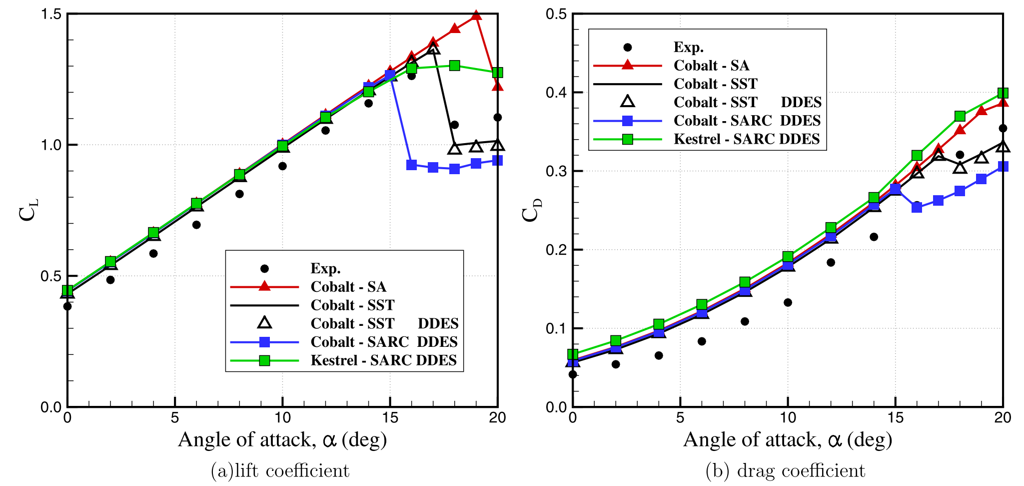

Fig. 6. Turbulence modeling effects on the CFD predictions of the bent and round wing. The mesh is coarse and half-geometry.

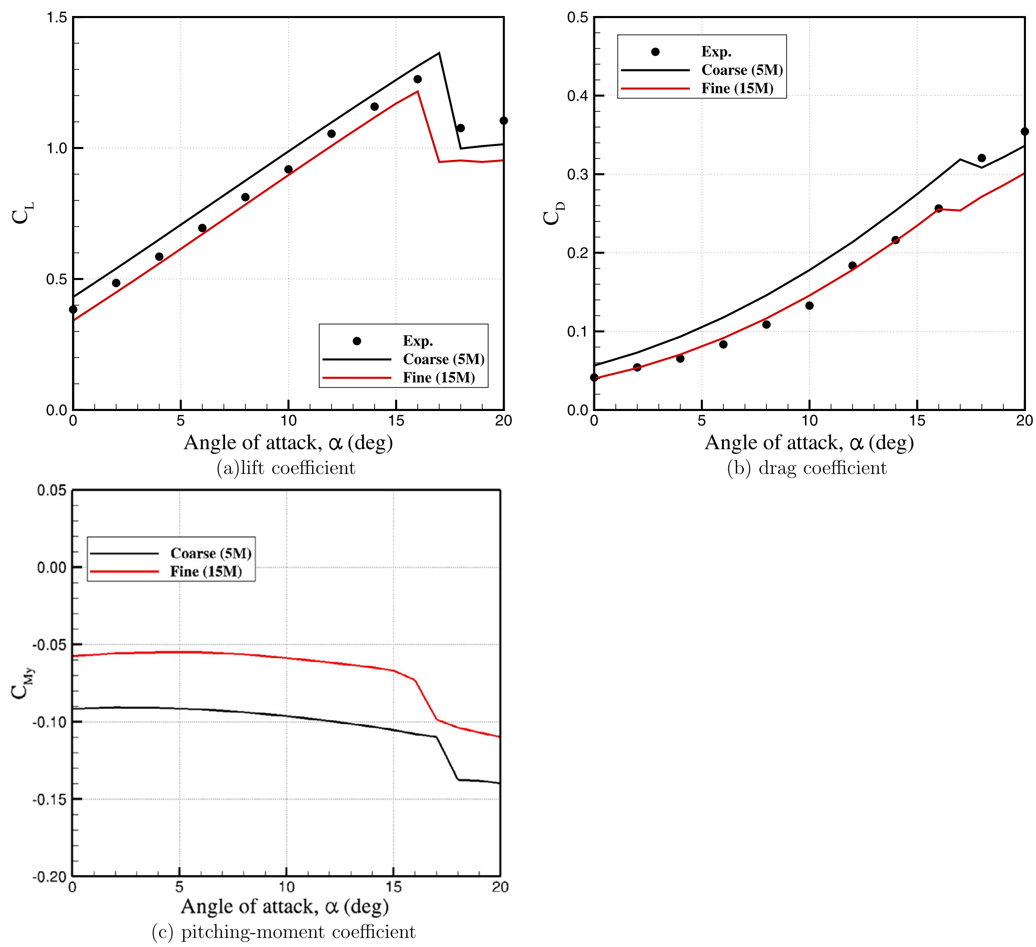

Fig. 7. Grid sensitivity study of the bent and round wing. All simulations ran with Cobalt using the SST turbulence model.

All fine meshes correspond to the full wings and have a left-side trailing-edge deflection. Inviscid tetrahedral meshes were generated by the ICEM-CFD code; these meshes were then used as a background mesh by the mesh generator of TRITET [36,37] which builds prism layers using a frontal technique. TRITET rebuilds the viscous mesh while respecting the size of the original inviscid mesh from ICEM-CFD. The closed-wing meshes have around 30 million cells and the open-wing meshes contain about 45 million cells. All meshes have a grid quality, as determined by the ICEM-CFD metric, above 90% which helps to accelerate the solution convergence.

5. Experimental setup

The static experiments of closed wings were performed in the SWT of USAFA. This closed-loop tunnel, shown in Fig. 5, has an 8 ft long test section with a test section cross-section of 3 ft by 3 ft. The tunnel can achieve speeds up to Mach 0.5. Bergeron et al. [34]

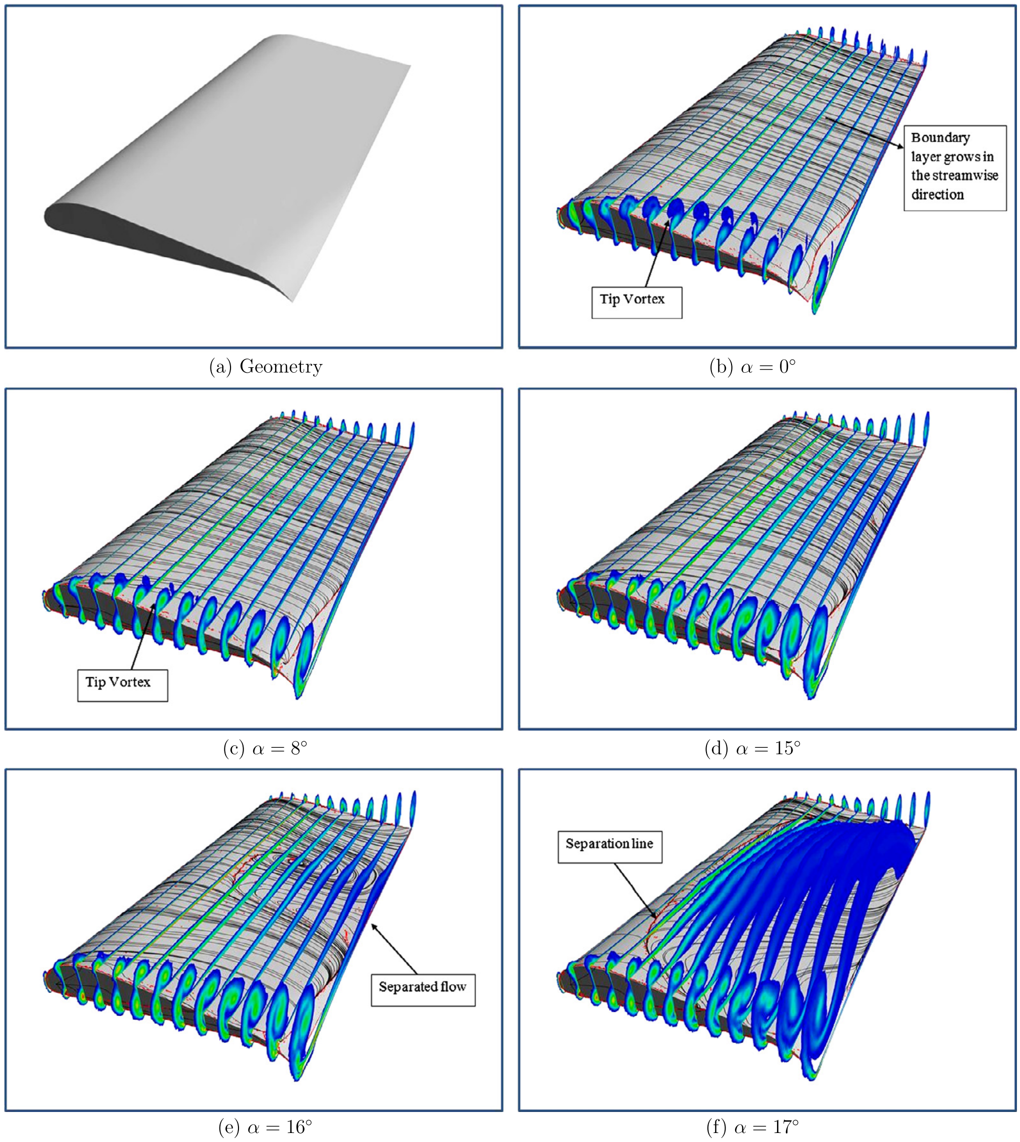

Fig. 8. Flow solutions of the BR wing using SST turbulence model. Iso-surfaces were created and colored by vorticity. The red lines show separation lines. (For interpretation of the references to color in this figure legend, the reader is referred to the web version of this article.)

detailed the experimental setup and data of ram-air parachutes. Four wing section configurations were fabricated to model two types of ram-air canopy control configurations, and two leading edge flow field behaviors. The experimental Reynolds number was 1.4×10^6. The lift and drag forces were measured by an external force balance installed under the SWT. The measurements reported for changes in angle of attack from zero to 20° with 2° increments below $\alpha = 8°$, and 1° increments above $\alpha = 8°$. These experimental data are used in this study to validate computational methods.

6. Results and discussion

The simulation conditions are $M = 0.25$ and $Re = 1.4 \times 10^6$ corresponding to the wind tunnel experiments. The moment reference point and rotation points are at the wing quarter chord. Number of 2,000 and 8,000 CFD time steps were used for static simulation of closed and open wings, respectively. In all static simulations, second-order accuracy in time and 3 Newton sub-iterations were used. The last 1,000 time step values were then averaged to obtain aerodynamic coefficients of open wings.

For dynamic simulations, five Newton sub-iterations with 2,000 time steps per cycle were used. The frequency in all motions is one Hz which corresponds to a reduced frequency of 0.01. This justifies the quasi-steady assumption required to estimate stability derivatives from these harmonic motions.

This section presents detailed results for several parameter studies including different turbulence models with an emphasis on building a flight dynamics database. These data supplement the data reported earlier in Bergeron et al. [15].

Fig. 6 compares CFD data of the coarse grid of the BR wing using a symmetry plane with experimental data. Four different turbulence models and two different flow solvers were investigated. The Cobalt flow solver was run with four turbulence models: Spalart–Allmaras (SA), Mentor's SST and Delayed Detached Eddy Simulation with SST and SA with Rotation Correction (SARC). Kestrel predictions using the DDES-SARC turbulence model are also shown in Fig. 6. All solutions converged to steady-state values. Fig. 6 shows that none of the CFD data match exactly with experiment; CFD data overestimate the lift and drag coefficients. Fig. 6 also shows that CFD data of both solvers and all turbulence models agree quite well with each other up to 15° angle of attack; the drag coefficient is slightly overestimated in Kestrel. However, CFD predictions are different above 15°. Cobalt with all used turbulence

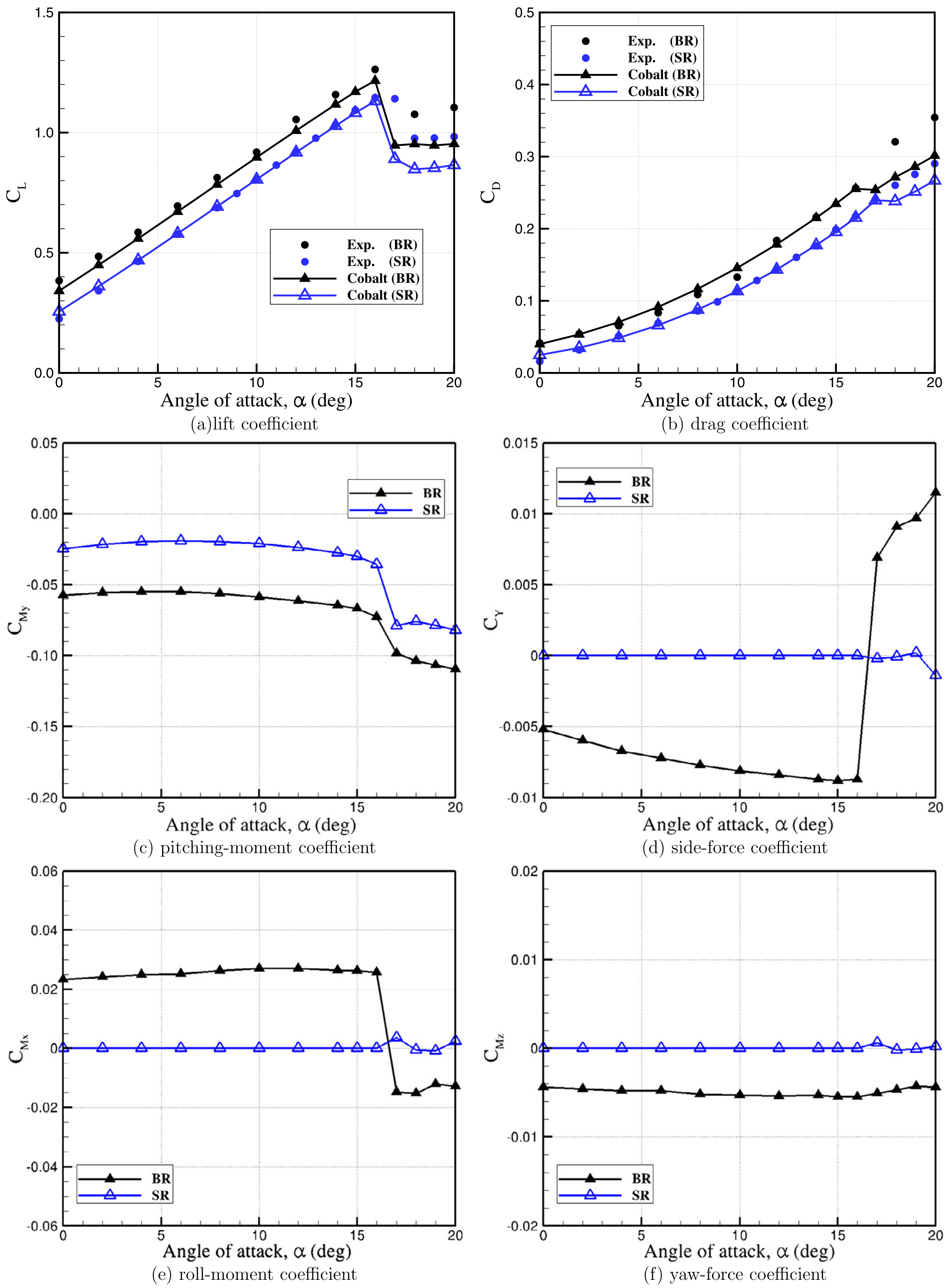

Fig. 9. Comparison of aerodynamic predictions of bent/round and straight/round wings. All simulations run with Cobalt using the SST turbulence model.

models predicts a sharp stall as the experiment does; Kestrel, on the other hand, predicts a smooth stall behavior. Fig. 6 shows that CFD data using the SST and DDES-SST turbulence model are similar for all angles of attack. The stall angle and post-stall curves significantly change with the turbulence model selection. The SA model predicts the stall too late and the DDES-SARC predicts it too early compared with experiments. The SST turbulence model predicts the stall at the correct angle. Therefore, the SST model was used for all subsequent simulations.

The coarse and fine mesh predictions of the BR wing are compared with experimental data in Fig. 7. These predictions are from Cobalt using the SST turbulence model. Fig. 7 again shows the CFD data of the coarse gird overestimate the experimental lift and drag coefficients. However, the predictions of the fine grid agree with experimental data very well up to the stall angle. The coarse grid predicts that the wing stalls at 17°; the stall angle is at 16° using the fine mesh. Fig. 7(c) also compares the pitching moment coefficients using the coarse and fine meshes. Though, the plot shapes look similar, the fine mesh predicts less negative pitching moment values than the coarse mesh. Note that the pitching moment curves have small positive or near zero curve slopes for small to moderate angles of attack. This is because the moment reference point is close to the wing's neutral point. Therefore, the BR wing has negative or neutral static stability in longitudinal direction.

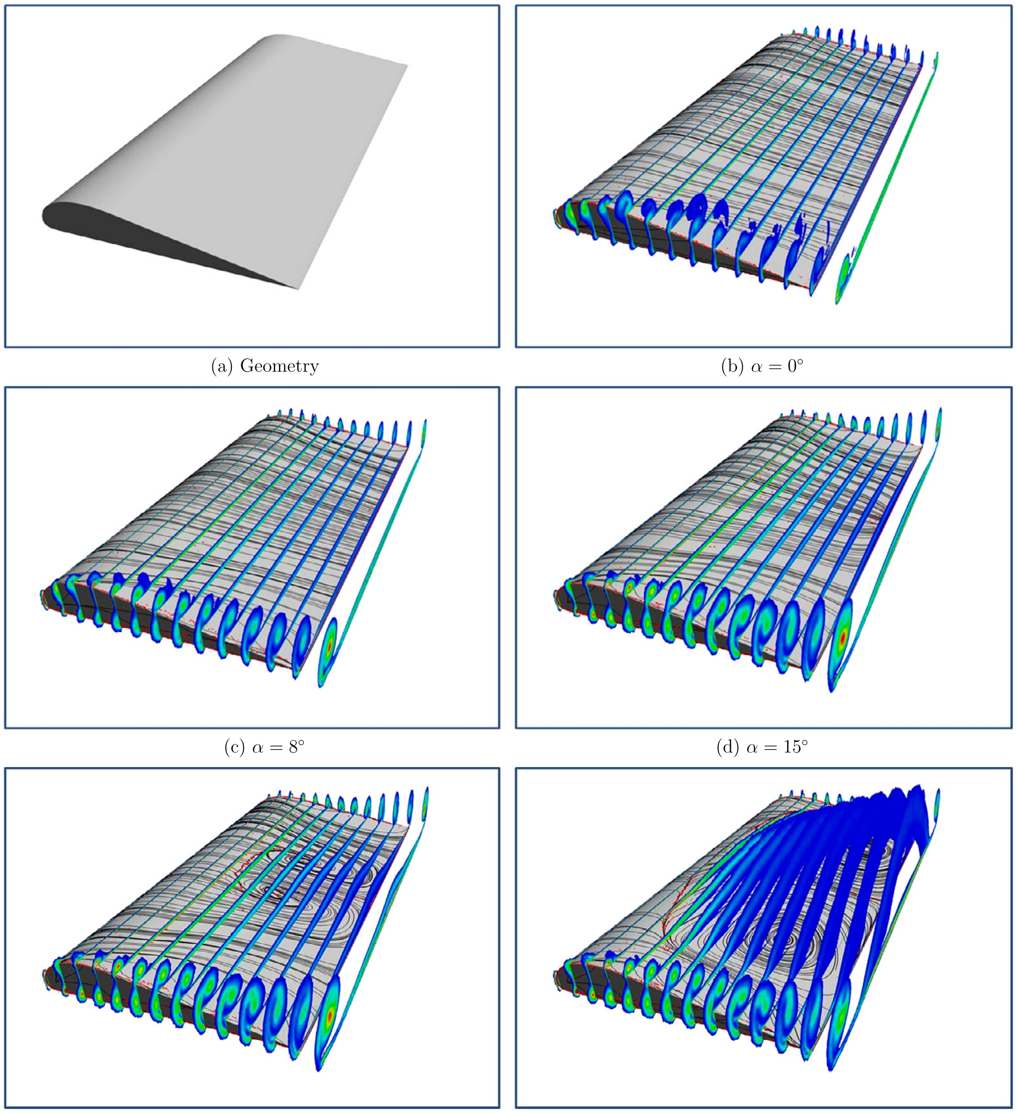

(a) Geometry (b) $\alpha = 0°$

(c) $\alpha = 8°$ (d) $\alpha = 15°$

(e) $\alpha = 16°$ (f) $\alpha = 17°$

Fig. 10. Flow solutions of the SR wing using SST turbulence model. Iso-surfaces were created and colored by vorticity. The red lines show separation lines. (For interpretation of the references to color in this figure legend, the reader is referred to the web version of this article.)

The flow solutions of the BR wing using SST turbulence model and the fine mesh are shown in Fig. 8 for various angles of attack. Vortices are formed at the wing tips; these vortices are slightly different due to straight and bent sides. Fig. 8 shows that wingtip vortices grow in size as they move downstream and as the angle of attack increases. Fig. 8 also shows that by increasing the angle of attack from 16° to 17°, a large separation region formed over the upper surface.

Cobalt predictions of the BR and SR wings are shown in Fig. 9 and compared with experimental data. All simulations correspond to fine meshes and the SST turbulence model. Fig. 9 shows that CFD data of both wings match very well with experiments up to stall angle. Bending the wing's left side downward causes the lift and drag to increase, and a nose down moment as shown in Fig. 9. Both wings show a stall angle of 17°. For the straight wing, all lateral coefficients are zero or nearly zero. However, the bent wing shows a negative side-force, a positive roll moment, and a negative yaw moment before stall. The lateral coefficients slightly change with the angle of attack and then show sudden changes as the wing stalls.

The flow solutions of the SR wing are shown in Fig. 10 for different angles of attack. The wingtip vortices can again be seen. Like the bent wing, the straight wing suddenly stalls at 17°. Furthermore, Fig. 11 compares the surface pressure of the bent and straight wings at angles of 8° and 15°. A low pressure region is formed over the upper surface upstream of the trailing edge bend. This low pressure region leads to increased lift, drag, and a nose-down pitching moment.

CFD simulations of the bent and straight wings were run for a sideslip angle sweep from −15° to 15° with an increment of 5°. The results are compared in Fig. 12 which shows a negative side-force curve slope with sideslip ($C_{Y\beta} < 0$), a negative roll-moment curve slope with sideslip ($C_{Mx\beta} < 0$), and a positive yaw-moment curve slope with respect to sideslip angle ($C_{Mz\beta} > 0$). These results confirm that both wings have positive static stability in lateral direction.

Next the results of the open wings with bent and straight trailing edges are shown. Like the closed wing, the bent side is on the left. CFD solutions of open wings took a long time to converge; this was previously experienced for open airfoils. Fig. 13 compares CFD data of open and closed wings. The comparison results show

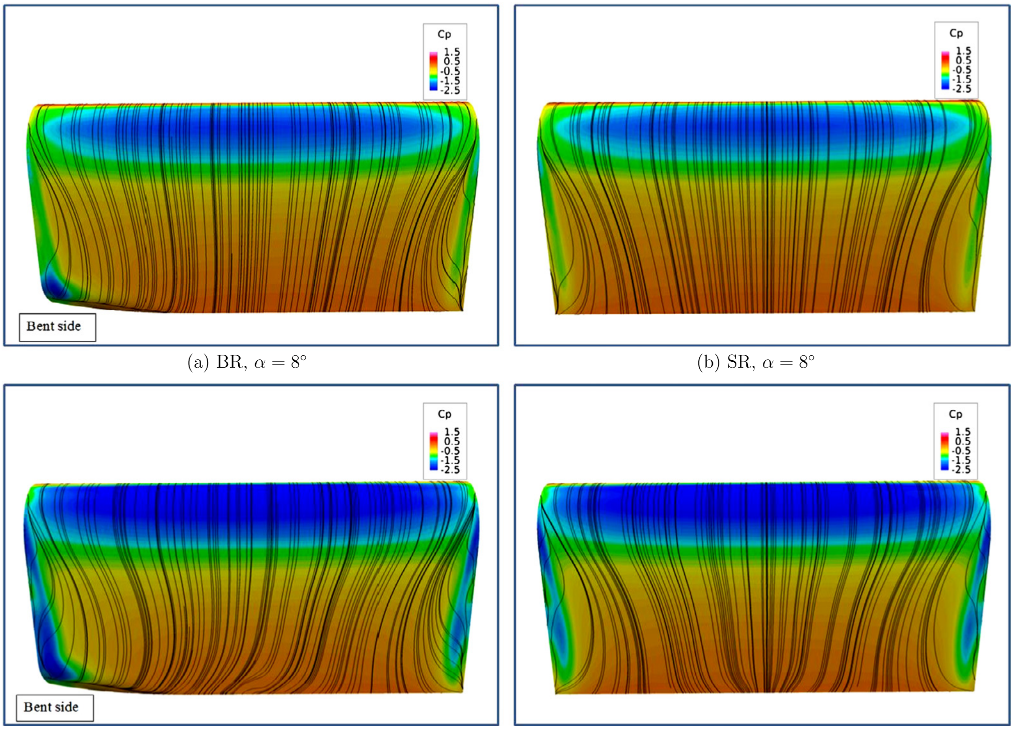

(a) BR, $\alpha = 8°$ (b) SR, $\alpha = 8°$

(c) BR, $\alpha = 15°$ (d) SR, $\alpha = 15°$

Fig. 11. Pressure solutions of the BR and SR wings using the SST turbulence model.

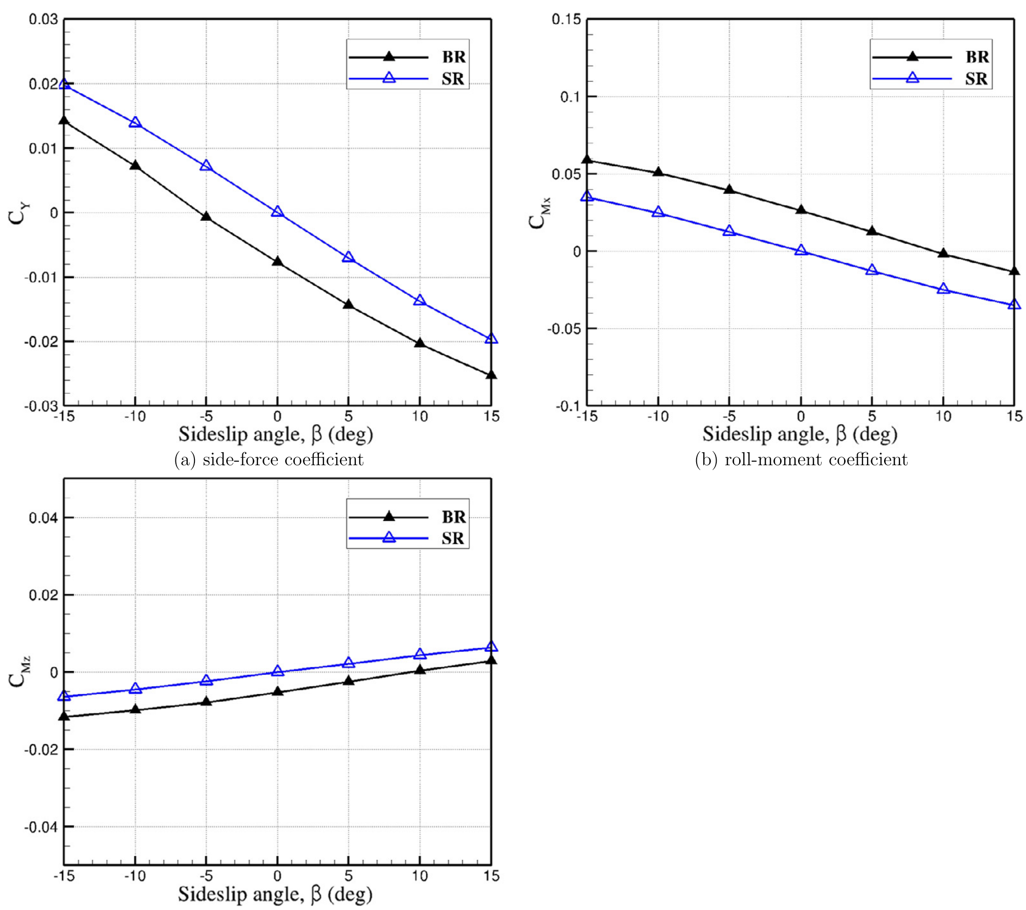

(a) side-force coefficient (b) roll-moment coefficient

(c) yaw-moment coefficient

Fig. 12. Lateral aerodynamic prediction of BR and SR wings at $\alpha = 8°$.

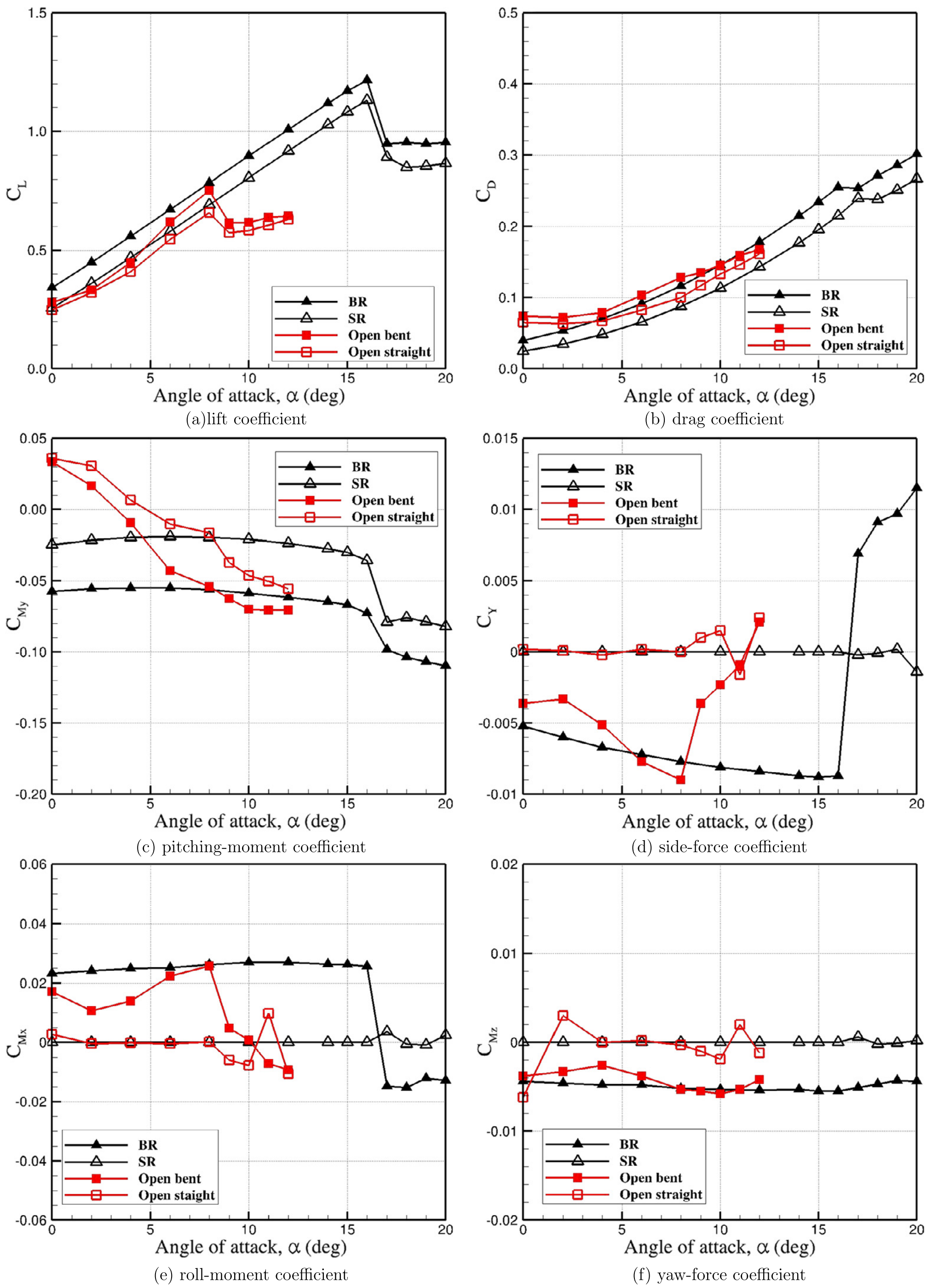

Fig. 13. Comparison of aerodynamic predictions of open and closed wings.

that the open wing has very nonlinear aerodynamic characteristics even at small angles of attack. The offset in curves due to a trailing-edge deflection varies with the angle of attack as well. The open wings stall at approximately 8°, much earlier than the closed wings. These wings have less lift and higher drag values compared with the closed wings, but they show a negative pitching moment curve slope and therefore provide a positive static stability in longitudinal direction. This is probably due to the open inlet section or the eddies formed at the lower surface. Fig. 13 shows that the open wing lateral coefficients are different from the closed-wings at small angles of attack; they become closer at higher angles and diverge after stall. Notice that the open wing with a straight trailing edge predicts non-zero lateral coefficients at small angles of attack.

Fig. 14 shows the time-averaged flow solutions of the open wings at angles of 0° and 8°. The figure shows that a large region of vorticity (eddy) is formed at the wing lower surface. This eddy is formed because of the sharp-edge exit of the flow inside cavity from the lower section. The air inside eddy is rotating counter-clockwise which decreases the surface pressure and thus changes aerodynamic coefficients. The eddy size changes with the angle of attack such that it becomes smaller with increasing angle of attack as shown in Fig. 14. As noted in Ghoreyshi et al. [17], at higher angles, a small eddy is formed on the upper surface near the leading

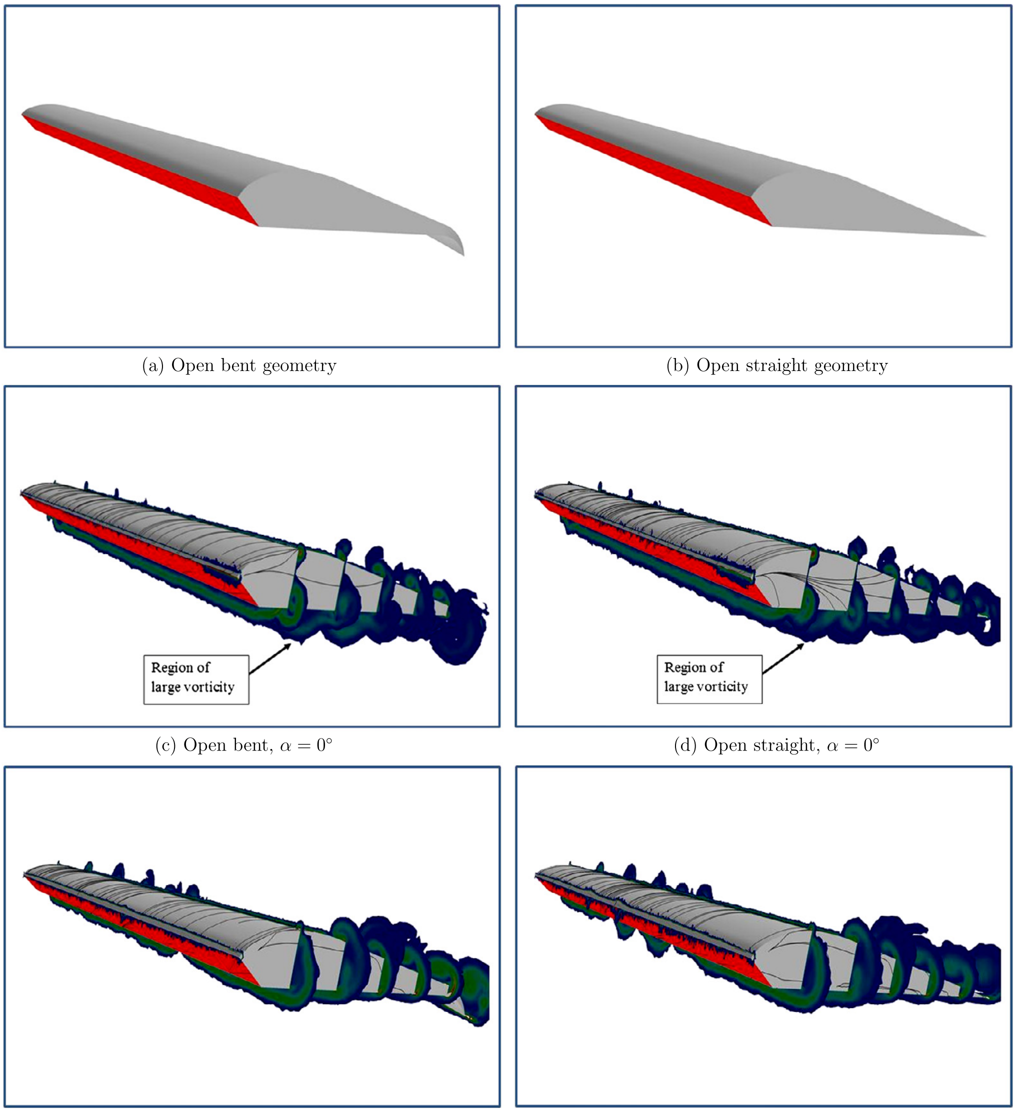

(a) Open bent geometry (b) Open straight geometry

(c) Open bent, $\alpha = 0°$ (d) Open straight, $\alpha = 0°$

(e) Open bent, $\alpha = 8°$ (f) Open straight, $\alpha = 8°$

Fig. 14. Flow solutions of open wings using SST turbulence model. The solutions were time-averaged over the last 1,000 iterations. Iso-surfaces were created and colored by vorticity. (For interpretation of the colors in this figure, the reader is referred to the web version of this article.)

edge as well. The upper surface flow is decelerated by this eddy, thus the flow separates from the upper surface earlier than on the closed-inlet geometry.

Final static results show the lateral aerodynamic characteristics of open wings for a sweep of sideslip angle at $\alpha = 8°$. These results are compared with the closed-wing data and are shown in Fig. 15. These comparisons show that closed and open wings have very similar lateral aerodynamic characteristics at $\alpha = 8°$. Both wings have positive static stability in the lateral direction as well.

The following figures show the dynamic solutions of the open and closed wings with a straight trailing edge. Both wings undergo simple harmonic motions in the yaw, pitch, and roll modes. The yaw and roll motions are at $\alpha = 8°$. The yaw motion is defined as $\beta = 2\sin(\omega t)$ with $f = 1$ Hz. Fig. 16 shows the lateral coefficients during the motion. The closed wing produces smooth, thin hysteresis loops; they are linear in shape as well. The open-wings show the loops in the same direction as the loops formed from the closed wing, but they show large oscillations during the motion. Note that the mean values nearly match with the closed wing results. These results show that the open wing solutions are unsteady and very sensitive to changes in sideslip angle.

Fig. 17 shows the lift, drag, and pitching moment coefficients during a pitch oscillation motion; the motion is defined as $\alpha = 6 + 2\sin(\omega t)$ with $f = 1$ Hz and at $\beta = 0$. The results show that hysteresis loops obtained from the open and closed wings are very different. The open wing has lower lift and higher drag coefficients. The lift data form a linear shape for both wings. While the closed-wing shows a linear-shape loop in the pitching moment, the open wing has a nonlinear shape as well.

The roll dynamic solutions are also shown in Fig. 18. The motion is defined as $\phi = 2\sin(\omega t)$ with $f = 1$ Hz at $\alpha = 8°$. Like the yawing motion, the open wing shows large oscillations in the aerodynamic coefficients. Apart from this, the loops from open and closed wings show similar mean values.

The linear regression method outlined in Section 2 was used to estimate the closed and open wing aerodynamic derivatives. The results are summarized and compared in Table 1. These derivatives show that both closed and open wings have nearly the same control derivatives. For both wings, bending the wing's left trailing edge downward causes the lift and drag to increase and the pitching moment to decrease. It also produces a small negative side force, a positive roll moment, and a small negative yaw moment. While open wings show large oscillations in aerodynamic

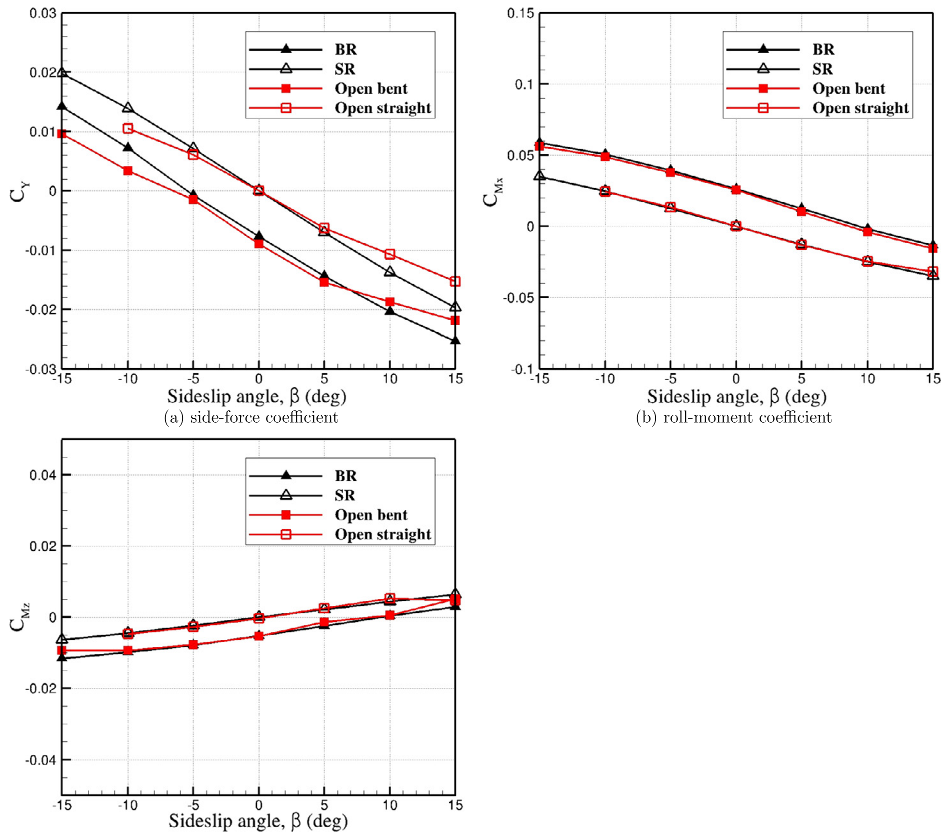

(a) side-force coefficient
(b) roll-moment coefficient
(c) yaw-moment coefficient

Fig. 15. Lateral aerodynamic prediction of open and closed at $\alpha = 8°$.

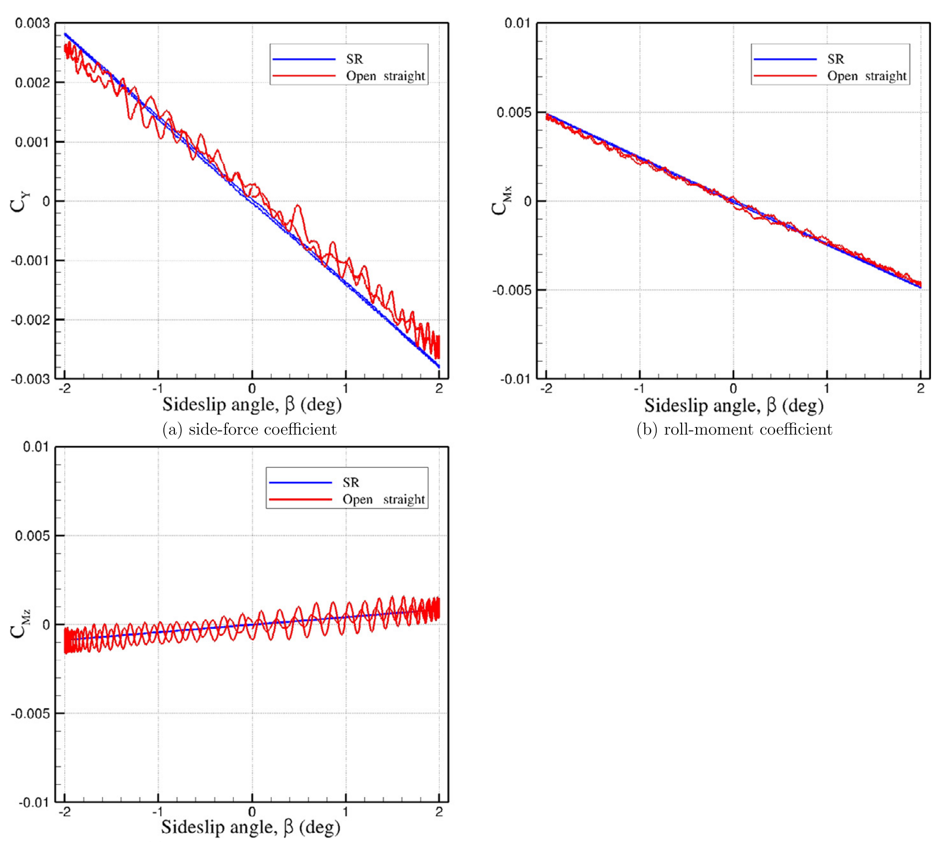

(a) side-force coefficient
(b) roll-moment coefficient
(c) yaw-moment coefficient

Fig. 16. Aerodynamic responses of open and closed wings to a yawing motion of $\beta = 2° \sin(\omega t)$ with $f = 1$ Hz at $\alpha = 8°$.

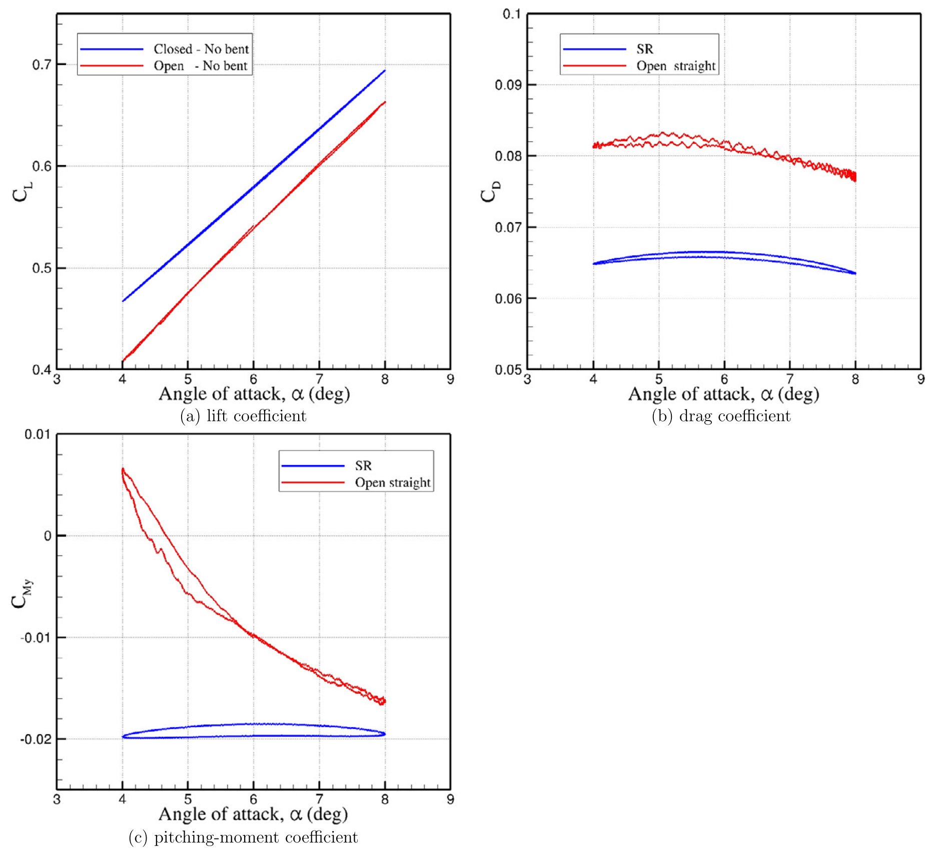

(a) lift coefficient (b) drag coefficient (c) pitching-moment coefficient

Fig. 17. Aerodynamic responses of open and closed wings to a pitching motion of $\alpha = 6° + 2° \sin(\omega t)$ with $f = 1$ Hz at $\beta = 0°$.

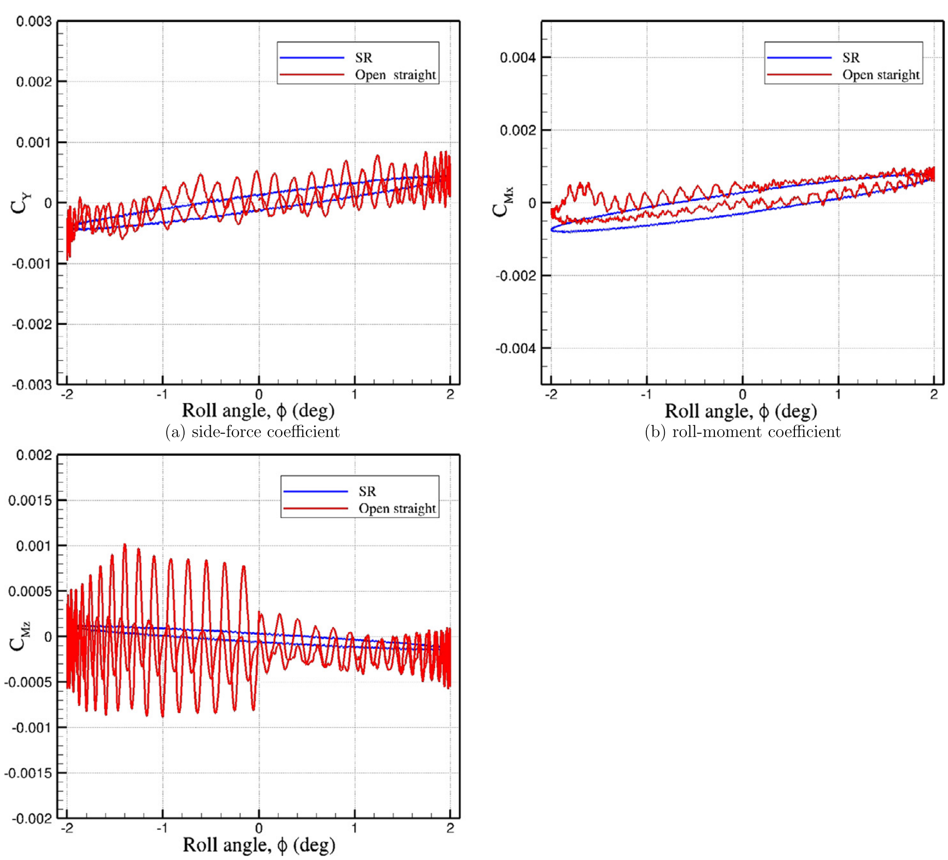

(a) side-force coefficient (b) roll-moment coefficient (c) yaw-moment coefficient

Fig. 18. Aerodynamic responses of open and closed wings to a rolling motion of $\phi = 2° \sin(\omega t)$ with $f = 1$ Hz at $\alpha = 8°$ and $\beta = 0°$.

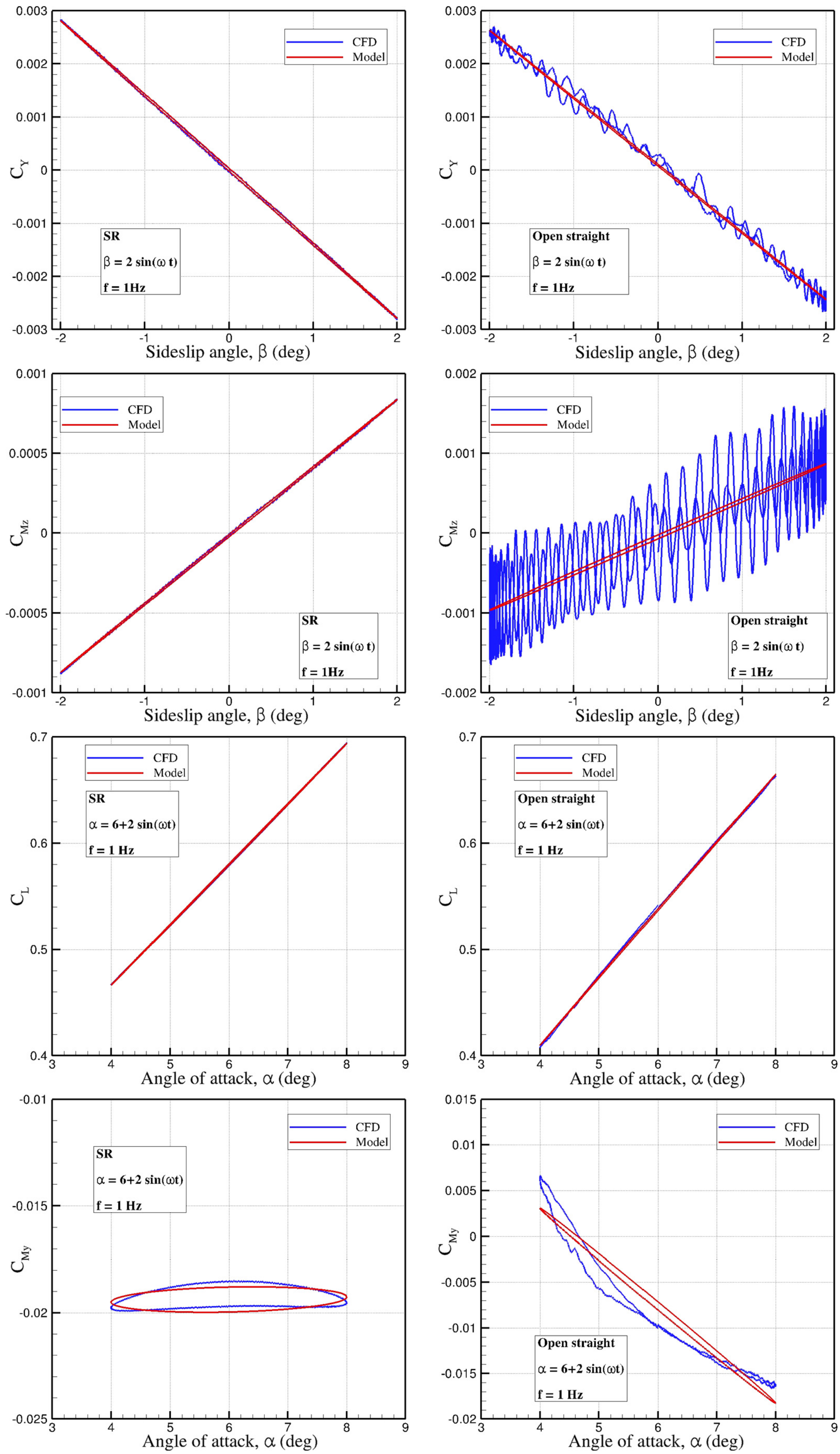

Fig. 19. Model predictions of yawing and pitching motions.

Table 1
Estimated aerodynamic derivatives at $\alpha = 8°$. For control derivatives, the left trailing edge is deflected downward. The moment reference point and rotation points are at the wing quarter.

Derivative (1/rad)	Closed-wing	Open-wing	Derivative (1/rad)	Closed-wing	Open-wing
$C_{L\delta}$	0.1171	0.0977	$C_{D\delta}$	0.0367	0.0321
$C_{Y\delta}$	−0.0098	−0.0101	$C_{Mx\delta}$	0.033	0.029
C_{My_δ}	−0.0465	−0.04036	$C_{Mz\delta}$	−0.00662	−0.00547
$C_{L\alpha}$	3.234	3.22	C_{My_α}	−0.04	−0.17761
$C_{Y\beta}$	−0.0802	−0.0722	$C_{Mx\beta}$	−0.144	−0.147
$C_{Mz\beta}$	0.0252	0.0286			
$C_{Yr} - C_{Y\dot{\beta}}$	0.036538	−0.025084	$C_{Mxr} - C_{Mx\dot{\beta}}$	−0.065654	−0.031794
$C_{Mzr} - C_{Mz\dot{\beta}}$	0.009994	0.032152			
$C_{Lq} + C_{L\dot{\alpha}}$	2.113513	2.368724	$C_{My_q} + C_{My_{\dot{\alpha}}}$	−1.521249	1.174727
C_{Yp}	−0.177494	−0.177494	C_{Mxp}	0.370360	0.358483
C_{Mzp}	0.060168	0.087783			

responses to yaw and roll motions, the aerodynamic derivatives with respect to yaw and roll rate of the open and closed wings are similar, in particular for roll-rate derivatives. However, the pitching moment derivatives with respect to pitch rate are very different in open and closed wings.

Aerodynamic models were created using derivatives given in Table 1 and were used to predict responses to some dynamic motions. Fig. 19 compares model and CFD data for these motions. Very good agreement was found for all motions of the closed wing. The model predictions of the open wing reasonably predict the mean CFD data but they do not predict oscillations observed in the CFD data. Discrepancies can be seen between model and CFD results in the pitching moment values during pitching motion. Note that open wing has nonlinear pitching moment behavior and therefore a model using linear regression method cannot fully predict.

7. Concluding remarks

This study presents a step towards bridging the gap between flight dynamics simulation of ram-air parachutes and high-fidelity computational fluid dynamics. The aerodynamic derivatives of open and closed wings were estimated using a linear regression method and training data from CFD simulations using small-amplitude oscillations in pitch, yaw, and roll directions. While the open wings have large oscillations in aerodynamic coefficients over the yawing and rolling hysteresis loops, lateral aerodynamic derivatives of the open and closed wings are similar. The results also show that model predictions are reasonably accurate for use in flight-dynamics simulations. Future work will extend these results to include and compare the flight dynamics simulation results from CFD and experimental data.

Conflict of interest statement

We wish to confirm that there are no known conflicts of interest associated with this publication and there has been no significant financial support for this work that could have influenced its outcome.

Acknowledgements

Mehdi Ghoreyshi and Jürgen Seidel are supported by USAFA; their financial support is gratefully acknowledged. Acknowledgments are expressed to the Department of Defense High Performance Computing Modernization Program (HPCMP) and the AFRL DSRC for providing computer time. The authors appreciate the support provided by the NSRDEC Airdrop Technology Team and the High Performance Computing Research Center at USAFA.

This material is based in part on research sponsored by the US Air Force Academy under agreement numbers FA7000-13-2-0009 and FA7000-13-2-0018. The U.S. Government is authorized to reproduce and distribute reprints for Governmental purposes notwithstanding any copyright notation thereon. The views and conclusions contained herein are those of the authors and should not be interpreted as necessarily representing the official policies or endorsements, either expressed or implied, of the US Air Force Academy or the U.S. Government.

References

[1] D.C. Jalbert, Multi-cell wing type aerial device, U.S. Patent No. 3,285,246.
[2] D. Poynter, The Parachute Manual: A Technical Treatise on Aerodynamic Decelerators, vol. 1, Para Publishing, Santa Barbara, CA, 1991.
[3] United States Government, US Federal Aviation Regulations, July 2012.
[4] J.D. Nicolaides, R.J. Speelman, G.L.C. Menard, A review of para-foil applications, J. Aircr. 7 (5) (1970) 423–431.
[5] V. Karlo, S. Aliabadi, W. Garrard, T. Tezduyar, S. Mittal, K. Stein, Parallel finite element simulation of large ram-air parachutes, Int. J. Numer. Methods Fluids 24 (1997) 1353–1369.
[6] G.E. Musgrave, A. Larsen, T. Sgobba, Safety Design for Space Systems, Elsevier Science, 2009.
[7] J.H. Strickland, H. Higuchi, Parachute aerodynamics: an assessment of prediction capability, J. Aircr. 33 (2) (1996) 241–251.
[8] S. Mittal, I.P. Saxena, A. Singh, Computation of two-dimensional flows past ram-air parachutes, Int. J. Numer. Methods Fluids 35 (2001) 643–667.
[9] N. Slegers, M. Costello, Aspects of control for a parafoil and payload system, J. Guid. Control Dyn. 26 (6) (2003) 898–905.
[10] J.S. Lingard, Precision aerial delivery seminar ram-air parachute design, in: 13th AIAA Aerodynamic Decelerator Systems Technology Conference, Clearwater Beach, May 1995.
[11] J.S. Lingard, The aerodynamics of gliding parachute, in: 9th AIAA Aerodynamic Decelerator Systems Technology Conference, AIAA Paper 1986-2427, May 1986.
[12] H. Mkrtchyan, H. Johari, Detailed aerodynamic analysis of ram-air parachute systems in steady flight, AIAA Paper 2011-2553, May 2011.
[13] K. Bergeron, M. Ward, M. Costello, Aerodynamic effects of parafoil upper surface bleed air actuation, AIAA Paper 2012–4737, August 2012.
[14] K. Bergeron, J. Seidel, M. Ghoreyshi, A. Jirasek, A.J. Lofthouse, R.M. Cummings, Numerical study of ram air airfoils and upper surface bleed-air control, AIAA Paper 2014-2832, June 2014.
[15] K. Bergeron, J. Seidel, M. Ghoreyshi, A. Jirasek, A.J. Lofthouse, R.M. Cummings, Computational fluid dynamics for the aerodynamic design and modeling of a ram-air parachute with bleed-air actuators, AIAA Paper 2015-0555, January 2015.
[16] M.A. Mohammadi, H. Johari, Computations of flow over a high performance parafoil, AIAA Paper 2009-2972, May 2009.
[17] M. Ghoreyshi, J. Seidel, K. Bergeron, A. Jirasek, A.J. Lofthouse, R.M. Cummings, Prediction of aerodynamic characteristics of a ram-air parachute, AIAA Paper 2014-2831, June 2014.
[18] M. Ghoreyshi, J. Seidel, K. Bergeron, A.J. Lofthouse, R.M. Cummings, Grid quality and resolution effects on the aerodynamic modeling of parachute canopies, AIAA Paper 2015-0407, January 2015.

[19] A. Eslambolchi, H. Johari, Simulation of flowfield around a ram-air personnel parachute canopy, J. Aircr. 50 (2013) 1628–1636.
[20] D.M. Cook, H.R. Adams, J. Seidel, CFD investigation of variable leading edge geometry and anhedral effects on ram air parachutes, United States Air Force Academy, December 2015, Applied cfd project.
[21] V. Klein, E.A. Morelli, Aircraft System Identification: Theory and Practice, AIAA Education Series, AIAA, Reston, VA, 2006.
[22] A. Khrabrov, K. Kolinko, A. Zhuk, I. Grishin, Wind tunnel test report, SimSAC Technical Report, October 2009.
[23] W.Z. Strang, R.F. Tomaro, M.J. Grismer, The defining methods of cobalt: a parallel, implicit, unstructured Euler/Navier–Stokes flow solver, AIAA Paper 1999-0786, 1999.
[24] J.J. Gottlieb, C.P.T. Groth, Assessment of Riemann solvers for unsteady one-dimensional inviscid flows of perfect gases, J. Fluids Struct. 78 (2) (1998) 437–458.
[25] R.F. Tomaro, W.Z. Strang, L.N. Sankar, An implicit algorithm for solving time dependent flows on unstructured grids, AIAA Paper 1997-0333, 1997.
[26] P.R. Spalart, S.R. Allmaras, A one equation turbulence model for aerodynamic flows, AIAA Paper 1992-0439, January 1992.
[27] D.C. Wilcox, Reassessment of the scale determining equation for advanced turbulence models, AIAA J. 26 (November 1988) 1299–1310.
[28] F. Menter, Eddy viscosity transport equations and their relation to the k–ε model, J. Fluids Eng. 119 (1997) 876–884.
[29] D. Post, Highlights of the CREATE program, in: Proceedings of the DoD HPCMP User Group Conference, Schaumburg, Ill., 2010.
[30] G.L. Roth, S.A. Morton, G.P. Brooks, Integrating CREATE-AV products DaVinci and Kestrel: Experiences and lessons learned, in: 50th AIAA Aerospace Sciences Meeting, Nashville, TN, 2012, No. AIAA-2012-1063.
[31] S.A. Morton, D.R. McDaniel, D.R. Sears, B. Tillman, T.R. Tuckey, Kestrel: a fixed wing virtual aircraft product of the CREATE program, in: 47th AIAA Aerospace Sciences Meeting, Orlando, FL, 2009, AIAA-2009-0338.
[32] T.J. Barth, D.C. Jespersen, The design and application of upwind schemes on unstructured meshes, AIAA Paper 89-0366, January 1989.
[33] B. vanLeer, J.L. Thomas, P.L. Roe, R.W. Newsome, A comparison of numerical flux formulas for the euler and Navier–Stokes equations, AIAA Paper 87-1104, 1987.
[34] K. Bergeron, J. Seidel, T. McLaughlin, Wind tunnel investigations of rigid ram-air parachute canopy configurations, AIAA Paper 2015-2156, March–April 2015.
[35] G.P. Brooks, J.W. Livingston, S. Adamec, W. McGough, HPCMP CREATE™ – AV DaVinci 3.0 and HPCMP CREATE™ – MG Capstone Integration, AIAA Paper 2015-1508, January 2015.
[36] L. Tyssel, Hybrid grid generation for complex 3D geometries, in: Proceedings of the 7th International Conference on Numerical Grid Generation in Computational Field Simulation, 2000, pp. 337–346.
[37] L. Tyssel, The TRITET grid generation system, in: Proceedings of the 10th International Conference on Numerical Grid Generation in Computational Field Simulations, International Society of Grid Generation (ISGG), 2000.
[38] Computational Research and Engineering Acquisition Tools And Environments (CREATE), Eglin AFB, FL 32542, Kestrel User Guide, Version 6.0, August 2015.